RSC Advances

PAPER

View Article Online
View Journal | View Issue

Cite this: *RSC Adv.*, 2025, **15**, 48325

Influence of laser ablation preparation of MgO and Bi_2O_3 nanoparticles on the optical and dielectric behavior of the PVA/PEO polymer blend

I. S. Elashmawi and A. A. Menazea *

Received 23rd October 2025
Accepted 19th November 2025

DOI: 10.1039/d5ra08147e

rsc.li/rsc-advances

This study aims to optimize the optical and electrical performance of polyvinyl alcohol/polyethylene oxide (PVA/PEO) incorporated with magnesium oxide (MgO) and bismuth(III) oxide (Bi_2O_3) nanoparticles synthesized by pulsed laser ablation over different durations. XRD revealed that the MgO nanoparticles acted as nucleating centers, increasing crystallinity. The incorporation of Bi_2O_3 resulted in sharper peaks and improved phase ordering with a prolonged ablation time. The FTIR spectra showed strong interactions between the PVA/PEO blend and nanoparticles, mediated by hydrogen bonding and novel vibrational modes between the metal and oxygen. UV-DRS showed optical modification and redshift of the absorption edge with a prolonged ablation time, indicating improved nanoparticle homogeneity, size growth, and crystallinity. TGA demonstrated an enhancement in the thermal stability of the Bi_2O_3/MgO double-filler composite. Dielectric and AC conductivity studies demonstrated a frequency behavior consistent with Maxwell–Wagner–Sillars interface polarization. Increasing the ablation time resulted in a decrease in the dielectric constant and conductivity, which was attributed to the small size and good dispersion of the nanoparticles and the restricted charge mobility due to the interface adhesion force.

1. Introduction

PVA and PEO are hydrophilic and biodegradable polymers that have garnered significant research interest because of their unique characterization and potential for blending.[1–5] PVA exhibits excellent film-forming properties, mechanical strength, biodegradability, chemical resistance, and biocompatibility.[6–8] The hydroxyl groups in the polymers form strong intermolecular and intramolecular hydrogen bonds, contributing to their crystallinity and mechanical stability. However, PEO is characterized by flexible ether linkages, high crystallinity, water solubility, and remarkable biocompatibility. The structural flexibility of PEO and the oxygen atoms along its backbone facilitate interactions with other polymers and can significantly influence its thermal and electrochemical behavior.[9–11]

Blending PVA and PEO aims to combine the beneficial characterization of both polymers into a composite material with enhanced mechanical flexibility, thermal stability, and functional versatility.[12] Hydrogen bonding interactions between the hydroxyl groups in PVA and the ether groups in PEO are crucial for their miscibility and phase behavior. These interactions promote partial miscibility within specific compositional ranges, which is typically reflected in changes in the glass transition and melting temperatures. Studies have indicated an enhance in the glass transition temperature and stabilization of the melting point, along with the formation of hydrogen bonds, as confirmed by spectroscopic methods such as FTIR. However, blends with a PEO content exceeding 30% often exhibit phase separation due to their limited miscibility, which negatively impacts the mechanical properties and contributes to brittleness.

TGA shows that PEO enhances the thermal stability of the blend by shifting the degradation stages to higher temperatures compared to pure PVA.[13] This is ascribed to the inherently high thermal stability of PEO and its ability to form stabilizing interactions with PVA. The blend typically undergoes degradation in three stages, including water evaporation and the main degradation process. Increasing the PEO content reduces the rate of weight loss and improves the overall stability of the blend. Mechanically, PEO acts as a plasticizer, which decreases the tensile strength but improves the elongation at break, thus enhancing the flexibility.[14,15] An optimal balance between the tensile strength and elongation is observed in blends containing approximately 25% PEO, which exhibit better polymer compatibility and less phase separation.[16]

Polymeric nanocomposites, manufactured by incorporating nanoscale fillers into polymer matrices, have revolutionized modern materials science due to their ability to significantly enhance characterization with minimal additions.[17–19] These engineered materials consist of polymers reinforced with nanoparticles, such as carbon nanotubes, metal oxides, or graphene, which typically range from 1 to 100 nanometers in at least one dimension and possess high aspect ratios. The

---

Spectroscopy Department, Physics Research Institute, National Research Centre, Dokki, Giza, 12622, Egypt. E-mail: aanter7@gmail.com

incorporation of these nanofillers dramatically improves a wide range of polymer characterization, including mechanical strength, stiffness, durability, thermal stability, and even biodegradability, while maintaining the inherent lightweight nature and processability of the original polymer. Achieving uniform dispersion and strong interfacial bonding between the polymer and the nanofillers is crucial, as poor dispersion or agglomeration can diminish the expected benefits, while well-dispersed nanofillers leverage their enormous surface area for synergistic effects.

Various synthesis techniques, such as *in situ* polymerization, solution mixing, and electrospinning, have been developed to address these challenges. The versatility and tunability of polymeric nanocomposites have facilitated their application in diverse systems, ranging from packaging and energy storage to aerospace, environmental remediation, and biomedical engineering. As innovations continue in nanotechnology and polymer processing, the future promises increasingly sophisticated nanocomposite systems with tailored functionalities, driving further advancements in high-performance, sustainable, and smart materials for technological and everyday applications.

The significance of this research lies in its exploration of the incorporation of MgO and Bi_2O_3 nanoparticles into PVA/PEO polymer blends using laser ablation, focusing on their effects on the spectral, structural, electrical, and dielectric properties. These nanocomposites hold promise for advanced applications in electronics, sensors, and energy storage due to their tunable electrical properties and enhanced functionalities. Understanding how these nanoparticles influence the charge transfer, polarization, and relaxation processes provides crucial insights for improving the material performance. This study also establishes a fundamental understanding of the electrical behavioral modifications induced by these nanofillers, which is essential for designing multifunctional composites. Therefore, this study contributes to the advancement of polymer nanocomposite engineering by linking nanoscale modifications to macroscopic electrical responses, paving the way for future studies.

In polymer nanocomposites, the properties under investigation are influenced by several factors. The polymer matrix's amorphous or crystalline nature governs the dipole orientation and charge mobility. Metallic materials and their composites are important materials that researchers have studied due to their various applications.[20–22] The addition of nano-fillers, such as MgO[23] and Bi_2O_3, enhances polarizability, disrupts crystallinity, and facilitates the formation of micro-capacitive regions. Furthermore, processing treatments, including techniques like laser ablation,[24,25] alter the microstructure, improve filler dispersion, and modify interface chemistry, thereby affecting the polarization mechanisms within the composite.

This study introduces a novel methodology for the preparation and utilization of magnesium oxide nanoparticles embedded within a PVA/PEO matrix, which is further integrated with bismuth oxide prepared *via* pulsed laser ablation for durations of 10, 20, and 30 minutes. The incorporation of magnesium oxide into this matrix is anticipated to significantly enhance the structural, optical, thermal, and electrical characteristics of the system. Moreover, it is expected that the electrical performance of the resulting composites will surpass that of both the pristine polymer blend and the blend containing only magnesium oxide. Comprehensive characterization of the PVA/PEO–MgO–Bi_2O_3 nanocomposites is conducted using X-ray diffraction, UV-DRS spectroscopy, Fourier-transform infrared spectroscopy, and electrical conductivity measurements.

2. Experimental work

2.1. Materials

The primary materials used in this study are polyvinyl alcohol (PVA, molecular weight ≈ 14 000; Merck, Germany) and polyethylene oxide (PEO, molecular weight ≈ 900; ACROS, New Jersey). Magnesium and bismuth plates with a purity of 99.99% were obtained from Sigma-Aldrich. All chemicals were used as received without further purification.

2.2. Preparation of PVA/PEO–MgO–Bi_2O_3 nanocomposite *via* laser ablation route

Equal weight ratios of PVA and PEO (50/50 by weight) were dissolved in double-distilled water while stirring at 60 °C until completely dissolved. Next, magnesium oxide (MgO) was added to the PVA/PEO polymer blend solution in a single step using laser ablation for 20 minutes. A beaker filled with 20 ml of PVA/PEO matrix solution and a pure magnesium plate was placed at the bottom of the beaker. Nanosecond laser ablation was used to create a laser ablation process using a convex lens placed in the path of the laser beam to focus on the magnesium target, thereby facilitating the synthesis of MgO NPs. The step of preparing magnesium nanoparticles in a PVA/PEO matrix is repeated 5 times to obtain 100 ml. Then, bismuth oxide (Bi_2O_3) is added to the previously prepared PVA/PEO–MgO solution in the form of a compressed bismuth pellet, again using laser ablation by the same procedure. Three concentrations of Bi_2O_3 were prepared using laser ablation times of 10, 20, and 30 minutes.

2.3. Characterization techniques

The structural characterization is determined by X-ray diffraction (XRD) with Cu Kα radiation using a Shimadzu 7000 diffractometer operating at 15 kV over a 2θ range of 4°–70°. Fourier Transform Infrared Spectroscopy (FT-IR) measurements were conducted in the wavenumber range of 400–4000 cm^{-1} using a Bruker VERTEX 70–70v spectrometer to analyze the infrared spectrum. UV-vis spectra were recorded using a JASCO V-630 double-beam spectrophotometer over the 190–1000 nm wavelength range. The surface morphology was examined using field emission scanning electron microscope (FESEM, QUANTA-FEG250, and Netherlands) under an operating voltage of 20–30 kV and was integrated with an EDX detector for examining the surface morphology and chemical composition of synthesized samples. Thermal stability was evaluated by thermogravimetric analysis (TGA) using a PerkinElmer TGA/7 instrument. High-frequency electrical conductivity measurements at room temperature were performed by employing a NOVOCONTROL Broadband Dielectric Spectroscopy (BDS) system (Model Concept-40). Measurements were conducted across a broad frequency spectrum, ranging from 0.1 Hz to 7 MHz, to comprehensively evaluate the frequency-dependent electrical behavior of the samples under study.

3. Results and discussion

3.1. X-ray diffraction

Fig. 1 depicts the X-ray diffraction (XRD) for the pristine PVA/PEO blend and the PVA/PEO composite containing magnesium oxide (MgO) nanoparticles synthesized *via* laser ablation for a duration of 20 minutes in the range of $2\theta = 4°–70°$. The XRD spectrum of the PVA/PEO blend features a broad, asymmetric diffraction peak centered around $2\theta \approx 19.59°$, with relatively low-intensity peaks extending across the spectrum. This pattern is typical of semicrystalline or amorphous polymers.[26]

Following the incorporation of magnesium oxide (MgO) nanoparticles prepared by laser ablation for 20 minutes, the XRD pattern exhibits significant structural changes compared to the original polymer blend. The main diffraction peak became sharper and more intense, indicating a significant increase in the overall crystallinity of the composite. Distinctive new small peaks are present within the 2θ range of approximately 35°–50°, which corresponds to the characteristic crystalline planes of magnesium oxide and reflects the successful integration and maintenance of the crystallinity of the magnesium oxide nanoparticles within the PVA/PEO matrix. The increased intensity and narrow shape of the main peak indicate the formation of crystalline microdomains, the nuclei of which are likely the embedded magnesium oxide nanoparticles. Furthermore, the core polymer peak may exhibit subtle shifts and distortions, indicating modifications in the packing order of the polymer chains and suggesting potential interface interactions between the polymers and the MgO domains. Several mechanisms combine to contribute to these observed structural transformations in the composite. Magnesium oxide nanoparticles act as effective nucleating agents, promoting the growth of ordered crystals within the PVA/PEO matrix by providing abundant nucleation sites through their high surface area, which reduces the activation energy required for crystallization and encourages the formation of fine crystalline regions. The MgO surface strongly interacts with polymer functional groups, particularly hydroxyl groups in PVA and ether oxygens, in facilitating preferential chain alignment, tighter molecular packing, and increased local order. Although magnesium oxide promotes crystallization, it simultaneously disrupts amorphous domains by creating microcapacitive interfaces and altering chain dynamics, resulting in a composite structure that includes well-ordered and disordered regions, as evidenced by the presence of sharp, broad diffraction features. In addition, using 20 minute laser ablation to prepare magnesium oxide nanoparticles results in the production of highly reactive nanocrystals with clean, defect-rich surfaces that intensify the interaction with the polymer and enhance its nucleation effect.

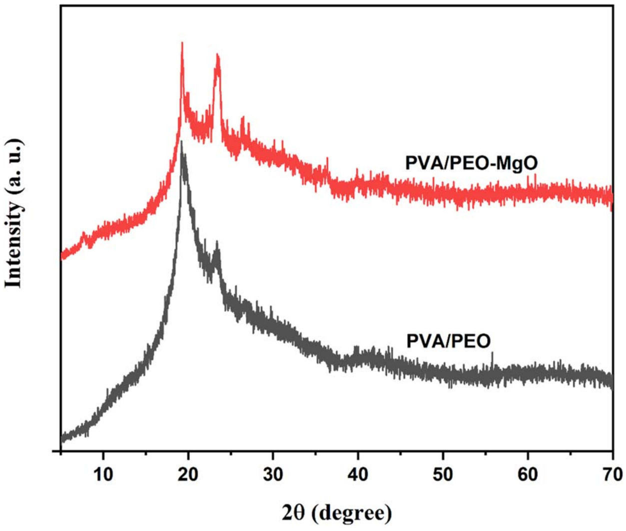

Fig. 1 X-ray diffraction (XRD) for the pristine PVA/PEO blend and the PVA/PEO composite containing magnesium oxide (MgO) nanoparticles synthesized *via* laser ablation.

Fig. 2 shows the XRD patterns of PVA/PEO–MgO doped with Bi_2O_3 nanoparticles prepared by laser ablation over different durations (10, 20, and 30 min). Across the spectra, diffraction peaks appear around several characteristic 2θ near 26°–28°, 30°–33°, and smaller peaks extending to 60°–70°. These sharp peaks correspond mainly to the crystalline phases of MgO and Bi_2O_3 nanoparticles, alongside background polymer broad humps from PVA/PEO. The strongest peaks around 28° potentially indicate the Bi_2O_3 crystalline planes, while peaks near 35–40° can relate to MgO crystalline reflections.

The intensity of these peaks generally increases from the 10 minute to the 30 minute ablation sample. The 30 minute spectrum features the highest intensity and sharpest peaks, suggesting enhanced crystallinity and possibly larger or more well-ordered nanoparticles. The 10 minute sample shows the lowest intensity and some peak broadening, indicating smaller or less crystalline nanoparticles.

At a 10 minute ablation, nanoparticle formation is in the early stages, leading to smaller crystallites and a less well-defined crystalline structure. The diffraction peaks show lower intensity and slight broadening, which is consistent with limited nucleation and growth. Dispersion may be more homogeneous with finely distributed nanoparticles but less crystallinity, impacting material properties like optical absorption and mechanical reinforcement. The 20 and 30 minute ablation diffraction patterns exhibit the highest peak intensity and sharpness. This implies substantial crystal growth of MgO and Bi_2O_3 nanoparticles with well-defined lattice planes visible in the XRD. The increased crystallinity likely affects the composite's physical properties, such as thermal stability and dielectric constant, due to stronger phase interactions and larger crystalline domains. However, excessive ablation may risk particle agglomeration, thus reducing homogeneity. Distinct XRD peaks confirm the successful doping of the PVA/PEO

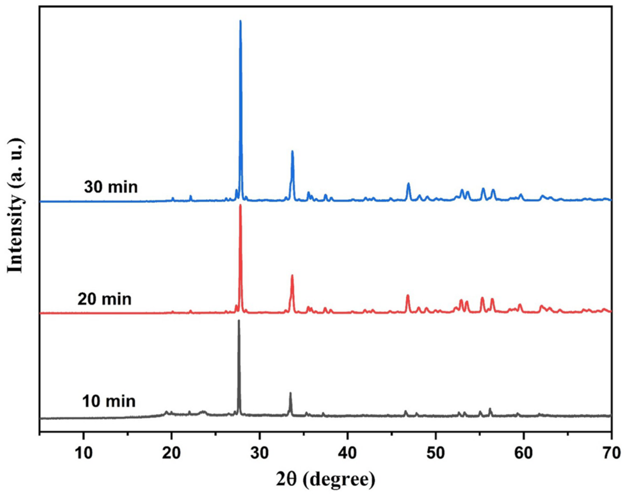

Fig. 2 XRD of PVA/PEO–MgO doped with Bi_2O_3 nanoparticles prepared by laser ablation over different durations (10, 20, and 30 min).

polymer with MgO and Bi_2O_3 nanoparticles synthesized by laser ablation. The presence of characteristic peaks rules out significant amorphous impurities or unwanted phases, affirming phase purity.

Laser ablation time serves as a tunable parameter for controlling nanoparticle size and crystallinity *in situ*. Short ablation times favor small nanoparticles with a high surface area but lower crystallinity, which is ideal for applications requiring nanoscale effects.

3.2. FT-IR

Fig. 3 depicts the FT-IR spectra for the pure PVA/PEO blend, PVA/PEO doped with MgO, and PVA/PEO–MgO doped with Bi_2O_3 (where Bi_2O_3 is doped by the duration of laser ablation processing (10, 20, and 30 minutes)). The spectrum of the pure PVA/PEO polymer blend shows that a broad band near 3300 cm^{-1} is attributed to O–H stretching from PVA. This reflects extensive hydrogen bonding. The shift or intensity changes of this band indicate altered hydrogen bonding environments. The prominent band near 2933 cm^{-1} corresponds to the C–H stretching of methylene and methyl groups from both PVA and PEO backbones.[10] The bands in the 1000–1500 cm^{-1} region are related to the C–O, C–C, and C–O–C vibrational modes. These bands represent C–O stretching and ether linkages, which are characteristics of the polymer's molecular structure.[26]

When MgO and Bi_2O_3 were incorporated into the polymer matrix, several spectroscopic changes are observed: a shift and broadening of O–H bands, indicative of new hydrogen bonding interactions between polymer hydroxyl groups and the MgO surface; the appearance of new absorption bands in the 500–700 cm^{-1} range corresponding to Mg–O stretching vibrations; and modifications within the fingerprint region, where broadened and shifted bands signify the formation of interfaces between the organic polymer and inorganic MgO domains. Additionally, a decrease in transmittance is often noted, which may result from nanoparticle-induced scattering effects. Table 1 shows the assignments to the FT-IR spectra and observations of the samples.

3.3. UV-DRS

Fig. 4 displays the ultraviolet-diffuse reflectance spectroscopy (UV-DRS) spectra for the PVA/PEO, PVA/PEO–MgO, and PVA/PEO–MgO–Bi_2O_3 nanocomposites prepared by laser ablation at 10, 20, and 30 minutes. The UV-DRS spectrum for the PVA/PEO blend shows very high reflection across the 210–450 nm wavelength range and reduces in the range from 450–1000 nm. Beyond 230 nm, the reflection decreases steadily, confirming that the blend is highly transparent in the visible and near-infrared regions.

Introducing MgO nanoparticles into the PVA/PEO blend, as shown in the reflection (R) spectrum of PVA/PEO–MgO composite, increases the material's reflection across UV and visible regions. MgO incorporation likely causes enhanced scattering centers and additional localized states within the band gap, promoting increased photon absorption. The polymer–nanoparticle interface acts as a localized site for electronic polarization, which amplifies light absorption and scattering.

The introduction of Bi_2O_3 nanoparticles into the PVA/PEO–MgO composite modifies the optical characteristics, as evidenced by the sharp reduce in reflection and distinct shifts in the absorption edge. When Bi_2O_3 nanoparticles are embedded in the polymer matrix, they introduce intermediate energy levels that facilitate sub-bandgap transitions, leading to an enhanced optical response. The laser ablation process allows fine control of nanoparticle generation time, size, and concentration.

At a 10 minute ablation period, the PVA/PEO–MgO–Bi_2O_3 composite exhibits moderate enhancement in UV reflection compared to MgO-only samples. The Bi_2O_3 nanoparticles generated during short ablation are small in size and fewer in number, leading to limited interfacial interactions. However, even at this stage, localized defect states begin to form,

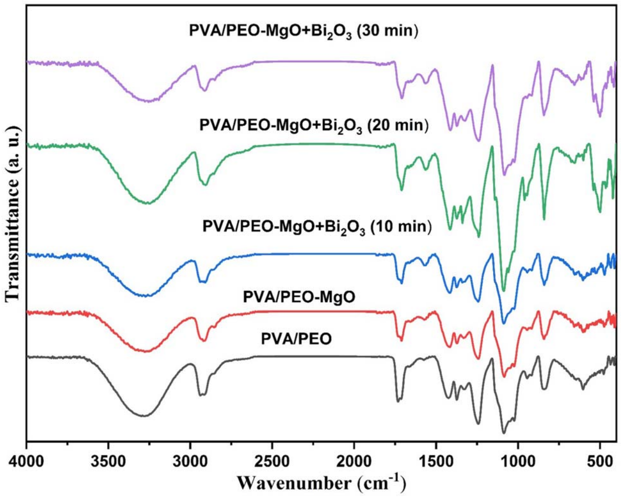

Fig. 3 FT-IR spectra for PVA/PEO, PVA/PEO–MgO, and PVA/PEO–MgO–Bi_2O_3 nanocomposites.

contributing to enhanced light absorption in the UV region. As the Bi_2O_3 nanoparticles ration increases in PVA/PEO, the reflection decreases in the wavelength range 210–450 nm. This intermediate ablation duration seems to provide an optimal balance between nanoparticle size and dispersion. The Bi_2O_3 nanoparticles at this stage act as efficient photo-absorption centers that facilitate charge transfer from the polymer matrix, enhancing the material's optoelectronic potential.

The optical band gap energy (E_g) is calculated using the Kubelka–Munk function, which relates the diffuse reflectance of a material to its absorption characteristics as follows:

$$F(R) = \frac{\left((1-R)^2\right)}{2R}, \tag{1}$$

where R is the reflectance and $F(R)$ represents the reflection coefficient. Fig. 5 illustrates the relationship between $(F(R)h\nu)^{1/2}$ and photon energy $h\nu$. The band gap energy (E_g) values are determined by extrapolating the linear portion of the curve to intersect the $h\nu$ axis at zero. A clear trend is observed where the optical band gap decreases as the filler content increases. This decrease is attributed to the ability of the nanofiller particles to self-organize within the polymer matrix, forming conductive pathways that facilitate electron hopping. These pathways cause shifts in both the valence band (VB) and conduction band (CB), enhancing carrier interactions within the material. As a result, the addition of nanofillers alters the energy levels of the samples, creating localized states within the forbidden band. These localized states can shift the Fermi level and serve as recombination and trapping sites, affecting the overall electronic properties. The modification of the band gap confirms that nanofillers play a significant role in tuning the optical and electronic behavior of the polymer composites.

3.4. FESEM and EDX

Fig. 6a–c shows the scanning electron microscopy (SEM) images and the energy-dispersive X-ray analysis (EDAX) of pure PVA/PEO, PVA/PEO–MgO, and PVA/PEO–MgO doped by Bi_2O_3 nanoparticles. The SEM image of a pure PVA/PEO polymer blend (Fig. 6a) reveals a fine-textured matrix interspersed with scattered spherical pores and some microcircular voids with one prominent, easily visible pore. The pores are mostly isolated, suggesting the presence of small vapor pockets formed during solvent evaporation.

The EDAX spectrum of a PVA/PEO (inset in Fig. 6a) exhibits strong peaks at low energy values, labeled with carbon (C) and oxygen (O), which are the two main constituents of PVA and PEO polymers. The dominance of the carbon and oxygen peaks confirms the presence of organic polymer components, as both PVA and PEO are primarily composed of carbon and oxygen atoms within their repeating units. Carbon is detected at a weight percentage of 27.29% and an atomic percentage of 33.33%, while oxygen is detected at a weight percentage of 72.21% and an atomic percentage of 66.67%, highlighting their important role in the polymer matrix.

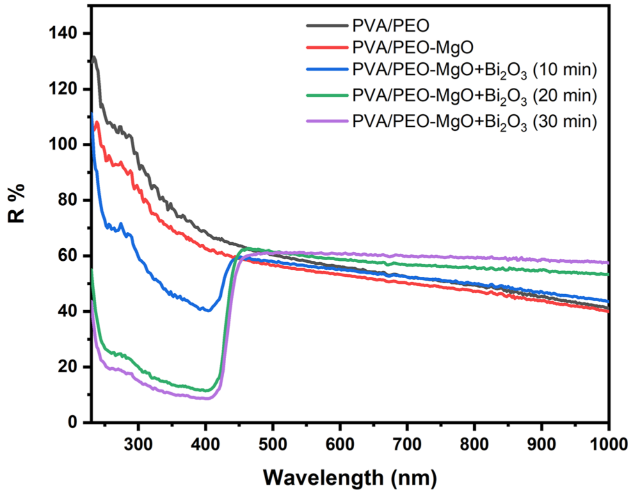

Fig. 4 Ultraviolet-diffuse reflectance spectroscopy (UV-DRS) spectra for the PVA/PEO, PVA/PEO–MgO, and PVA/PEO–MgO–Bi_2O_3 nanocomposites.

The FESEM image of the PVA/PEO incorporated with MgO, as shown in Fig. 6b, reveals a marked change in surface morphology compared to the original mixture. Unlike the smooth and homogeneous nature of pure PVA/PEO, the saturated sample exhibits a distinct dispersion of shiny granular aggregates on the surface, indicating the presence of MgO nanoparticles embedded in the polymer matrix. These aggregates vary in size and uneven distribution, forming fine clusters in some areas. Furthermore, the presence of MgO appears to disrupt the otherwise continuous polymer network, adding new roughness and contrast. The surface no longer possesses the isolated pores typical of unsaturated mixtures but instead displays numerous protrusions and small clusters that could represent nucleation points or reaction sites. The EDAX spectrum (inset in Fig. 6b) clearly shows elemental peaks for O, C, and Mg. Oxygen predominates at 71.51% wt%, representing contributions from both the polymer matrix and the MgO. Carbon accounts for 26.30% wt%, indicating a robust organic structure. The presence of magnesium (2.18% wt%) confirms

Table 1 FT-IR spectral assignments and observations of the samples

Wavenumber (cm^{-1})	Assignment	Observed in the samples
∼3300	O–H stretch	All, shifts with MgO, Bi_2O_3
∼2900	C–H stretch	All
1000–1500	C–O, C–C, C–O–C	All, broadened with fillers
700–800	Bi–O, Mg–O stretch	MgO, higher in the Bi_2O_3 samples
500–700	Mg–O, Bi–O–Bi	Most pronounced at high Bi_2O_3

the successful incorporation of the MgO nanoparticles into the matrix.

An FESEM image of the PVA/PEO–MgO doped by Bi_2O_3 nanoparticles (Fig. 6c) reveals a dramatic transformation in surface morphology. The polymer matrix appears rich in highly dispersed, rod-shaped, and needle-shaped crystalline particles, reflecting the successful integration and interaction of the MgO and Bi_2O_3 nanoparticles within the blend. The nanofillers are uniformly distributed across the surface, forming a continuous composite network rather than isolated clusters. This extensive dispersion increases surface roughness and creates a fine-textured structure across the entire film. The Bi_2O_3 particles appear well integrated, minimizing the large voids or phase-separated domains typically found in unsaturated blends. This structure enhances the surface interaction between the nanoparticles and the polymer chains, improving the mechanical properties, conductivity, and thermal stability of the composite. High-altitude, well-organized nanocrystals may also facilitate new pathways for ion transport. The EDAX spectrum (inset in Fig. 6c) is characterized by dominant peaks of O, C, and Mg, as expected from the base matrix, but also exhibits distinct Bi peaks at higher energies, characteristic of doped samples. Quantitative analysis maintains O (71.51%) and C (26.30%) as the main components, while Mg (2.18%) signals remain visible from MgO. The multiple Bi peaks confirm the presence and distribution of Bi_2O_3 nanoparticles throughout the sample.

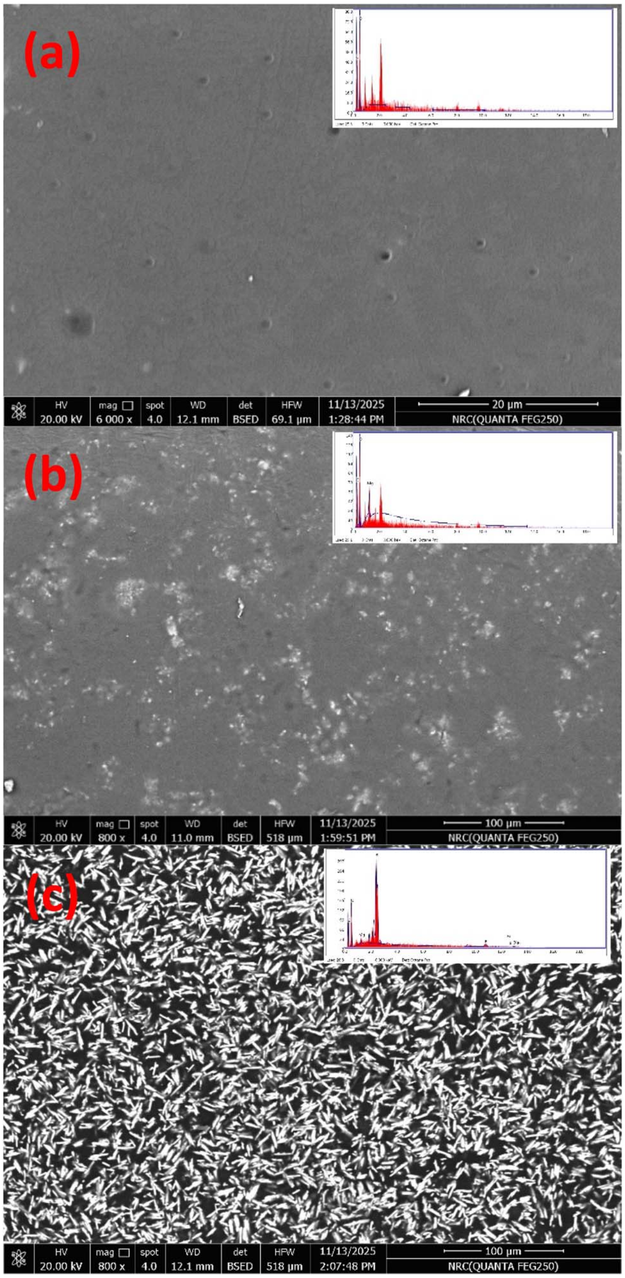

Fig. 6 (a–c) FESEM images and EDAX of (a) pure PVA/PEO, (b) PVA/PEO–MgO, and (c) PVA/PEO–MgO doped by Bi_2O_3 nanoparticles.

3.5. Thermogravimetric analysis (TGA)

TGA is a primary method for assessing the thermal stability, decomposition stages, and residue content of polymers and their composites. For PVA/PEO blends and their MgO/Bi_2O_3 nanocomposites, TGA elucidates how nanofiller inclusion, dispersion quality, and ablation conditions modify degradation temperature zones and char yields. Fig. 7 illustrates the TGA thermograms for PVA/PEO polymer blend, PVA/PEO–MgO composite (MgO prepared by laser ablation at 20 min), and PVA/PEO–MgO doped by Bi_2O_3 nanoparticles prepared by laser ablation at 10, 20, and 30 min.

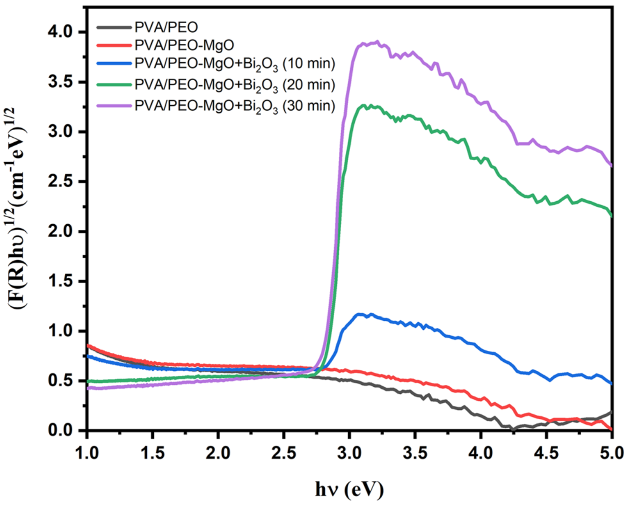

Fig. 5 Relationship between $(F(R)h\nu)^{1/2}$ and the photon energy $h\nu$ for PVA/PEO, PVA/PEO–MgO, and PVA/PEO–MgO–Bi_2O_3 nanocomposites.

The thermogram, representing a pure PVA/PEO blend, serves as a thermal stability reference. Initial mass remains stable up to roughly 200 °C, which is attributed to the evaporation of absorbed moisture and minor loss of volatile species. The primary decomposition phase occurs between 250 °C and 400 °C, relating to PVA/PEO chain scission and breakdown of the polymer structure. Beyond ~450 °C, mass loss plateaus leave a small residue at 700 °C, indicating polymer carbonization and residual mineral content. Blending PVA and PEO changes the thermal behavior relative to pure polymers. Intermolecular hydrogen bonding and molecular compatibility increase thermal resistance and shift the major decomposition steps to slightly higher temperatures.

For PVA/PEO–MgO, MgO inclusion provides modest improvement in thermal stability, visible as a delayed onset of major mass loss and a slightly higher final residue. The decomposition steps mirror the polymer blend but with increased resistance to weight loss in the main 300–400 °C zone.

This effect is attributed to the strong physical barrier and heat sink properties of MgO nanofillers, which impede thermal energy transfer and promote char formation. The nanoparticles interact with the polymer chains, creating tortuous diffusion paths for volatile fragments and stabilizing the matrix against rapid degradation. Well-dispersed MgO leads to maximum improvement, while agglomeration negates this effect. The shoulder differentiating the composite curve from the pure blend confirms enhanced thermal resistance and integration of the nanofiller through effective laser ablation.

The incorporation of Bi_2O_3 nanoparticles into the PVA/PEO–MgO matrix significantly shifts the major mass loss events toward higher temperatures, as indicated by flatter and more gradual transitions within the 250–450 °C decomposition range. Samples subjected to extended ablation periods of 20 and 30 minutes exhibit superior thermal stability, evidenced by a delayed onset of major decomposition and higher residual weight above 600 °C. This enhancement is attributed to Bi_2O_3's barrier effect, which hinders heat and volatile diffusion, and its chemical interaction with polymer chains, leading to improved cross-link density. Longer ablation times produce smaller, well-dispersed nanoparticles, maximizing char formation, while shorter ablation (10 min) yields a modest improvement, emphasizing the influence of particle size and distribution on stability.

The TGA thermograms reveal three distinct thermal regions: an initial minor weight loss below 200 °C associated with moisture or volatile removal, which remains minimal across all samples due to pre-drying and the low hydrophilicity of polymers; a major decomposition stage between 250 and 450 °C corresponding to the breakdown of PVA and PEO chains, where nanocomposite samples display a slower mass loss rate and higher degradation onset; and a final plateau between 450 °C and 700 °C representing char formation and inorganic residue. The highest residual mass at 700 °C is observed for the PVA/PEO–MgO–Bi_2O_3 composite ablated for 30 minutes, indicating optimal nanofiller incorporation and enhanced structural stability within the polymer matrix. The MgO-only composite already improves thermal performance over the base blend; however, the synergistic addition of Bi_2O_3 (especially at longer ablation times) enhances this effect. Together, they further restrict mass loss, increase residue, and provide multi-phase stabilization, which is beneficial for applications demanding fire resistance or extended service at elevated temperatures.

3.6. Determination of activation energy (E)

The activation energy (E) can be determined using the integral equation of Coats and Redfern for the TGA thermal decomposition measurements. For a first-order reaction (which models many polymer decomposition processes), depending on the residual mass, the equation is as follows:[27]

$$\ln\left[\frac{1-(1-\alpha)^{1-n}}{T^2}\right] = \ln\frac{R}{\Delta E}\left[1-\frac{2RT}{E}\right] - \frac{1}{2.303}\frac{E}{RT}, \quad (2)$$

where T is the absolute temperature, E is the activation energy in J mol^{-1}, R is the universal gas constant, n is the order of reaction, and α is the fractional weight loss at that particular temperature, calculated as follows:[28]

$$\alpha = \frac{w_i - w_t}{w_i - w_f}, \quad (3)$$

where w_i is the initial weight, w_t is the weight at a certain temperature, and w_f is the final weight of the sample. For $n \neq 1$, eqn (2) reduces to ref. 29

$$\log\left[\frac{-\log(1-\alpha)}{T^2}\right] = \log\frac{R}{\Delta E}\left[1-\frac{2RT}{E}\right] - \frac{1}{2.303}\frac{E}{RT}. \quad (4)$$

For each sample, we plot the relation between $-\log\left[\frac{-\log(1-\alpha)}{T^2}\right]$ against reciprocal temperature $\left(\frac{1000}{T}\right)$, and we obtain a straight line, as shown in Fig. 8. The estimated values of activation energy (E) are obtained from the slope of the plot as follows:

$$E = 2.303R \times \text{slope}. \quad (5)$$

The calculated value of the activation energies of the samples is shown in Table 1. It is observed that the values of the activation energy were 70.3, 71.9, 65.4, 63.6, and 62.3 kJ mol^{-1} for PVA/PEO, PVA/PEO–MgO, PVA/PEO–MgO + Bi_2O_3 (at 10 min), PVA/PEO–MgO + Bi_2O_3 (at 20 min), and PVA/PEO–MgO + Bi_2O_3 (at 30 min), respectively, indicating that the filler intensively affects the polymer.

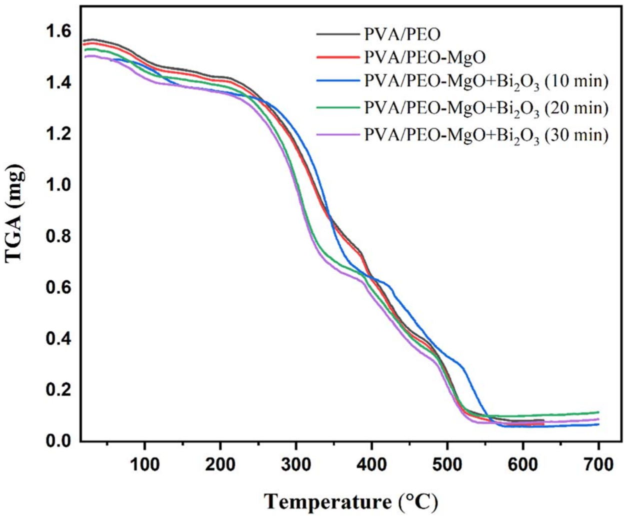

Fig. 7 TGA thermograms for PVA/PEO, PVA/PEO–MgO, and PVA/PEO–MgO–Bi_2O_3 nanocomposites.

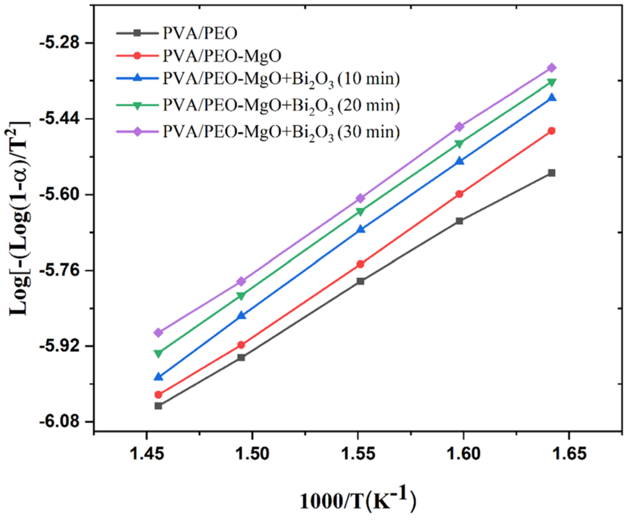

Fig. 8 Relation between $-\log\left[\frac{-\log(1-\alpha)}{T^2}\right]$ against reciprocal temperature $\left(\frac{1000}{T}\right)$ for PVA/PEO, PVA/PEO–MgO, and PVA/PEO–MgO–Bi_2O_3 nanocomposites.

The addition of MgO slightly increases the activation energy, indicating a stabilizing effect and improved thermal resistance, likely due to stronger intermolecular bonding and thermal insulation in the PVA/PEO matrix. In contrast, Bi_2O_3 addition reduces the activation energy possibly by catalyzing decomposition or increasing chain mobility, which makes the polymer blend easier to break down. Longer soaking times further lower the activation energy, suggesting an enhanced interaction or dispersion of Bi_2O_3, thereby facilitating polymer decomposition through structural disruption or defect formation.

3.7. AC conductivity

Fig. 9 illustrates the variation of the dielectric constant (ε') as a function of the logarithm of frequency ($\log f$) for the pure PVA/PEO blend, PVA/PEO doped with MgO, and PVA/PEO–MgO and Bi_2O_3 (where Bi_2O_3 is doped by the duration of laser ablation processing (10, 20, and 30 minutes)) at room temperature. At low frequencies, the dielectric constant is typically the highest, reflecting the dominant contribution of interfacial polarization, space charge accumulation, and maximum dipole alignment with the field.[30] At high frequencies, the dielectric constant drops as dipoles can no longer respond quickly to the oscillating field.

The real (ε') and imaginary (ε'') components of the dielectric constant, the AC conductivity (σ_{ac}), and the complex electric modulus (M^*) are respectively calculated using the following formulas:[27]

$$M^* = M' + iM'', \tag{6}$$

$$M' = \frac{\varepsilon'}{\varepsilon'^2 + \varepsilon''^2}, \tag{7}$$

$$M'' = \frac{\varepsilon''}{\varepsilon'^2 + \varepsilon''^2}, \tag{8}$$

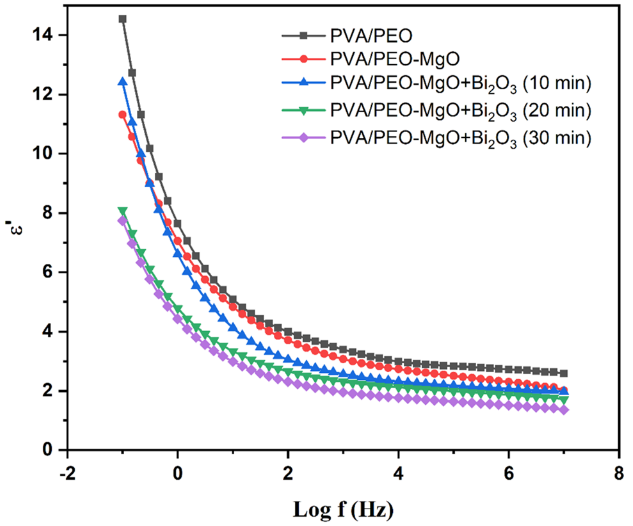

Fig. 9 Variation of the dielectric constant (ε') as a function of $\log f$ for PVA/PEO, PVA/PEO–MgO, and PVA/PEO–MgO–Bi_2O_3 nanocomposites.

$$\sigma_{ac} = 2\pi\varepsilon_o\varepsilon' \tan\delta, \text{ where } \tan\delta = \frac{\varepsilon'}{\varepsilon''}. \tag{9}$$

All curves show a steep decline in the dielectric constant with increasing $\log f$, followed by a leveling off at high frequencies. The high value of ε' observed at a low frequency is due to significant polarization charges fully align with the applied field, maximizing dielectric storage. The decline in ε' at higher frequency is attributed to charges and dipoles that cannot follow the rapid field reversals, leading to decreased effective polarization, and the curves flatten at high frequency, which is a response that becomes dominated by intrinsic electronic polarization, with minimal contribution from slower processes. The pure PVA/PEO blend exhibits the largest values of ε' across most frequencies.[27] In the absence of inorganic fillers, the polymer chains in PVA/PEO retain greater flexibility and segmental motion, facilitating efficient dipole orientation at low frequencies. Bi_2O_3 nanoparticles interact with the PVA/PEO polymer matrix at the molecular level primarily through hydrogen bonding and dipole–dipole interactions with the hydroxyl groups in PVA and the ether groups in PEO. These interactions alter the local polymer chain dynamics and modify the microenvironment surrounding the nanoparticles. Consequently, the Bi_2O_3 nanoparticles establish effective charge-trapping sites at the polymer–nanoparticle interfaces, significantly influencing the charge distribution. This interfacial region acts as a barrier to charge carrier migration, slowing down relaxation processes, which are reflected in the prolonged relaxation times observed in dielectric measurements. The presence of MgO and Bi_2O_3 nanoparticles further enhances dielectric behavior by introducing multiple heterogeneous interfaces within the composite. MgO, known for its dielectric strength and mechanical reinforcement, provides additional polarization centers. Bi_2O_3 also enhances charge retention and interface polarization resulting from permittivity and conductivity anisotropy at the interfaces, leading to a pronounced Maxwell–Wagner–Sillars effect. These nanoparticles work synergistically to improve dielectric permittivity, stability, and relaxation dynamics, with complex interactions between the polymer and the nanoparticles balancing charge transfer and dipole relaxation to enhance overall dielectric properties.

Fig. 10 illustrates the frequency dependence of the real part (the dielectric modulus, M') of the prepared samples. The dielectric modulus (M^*) is a powerful analytical approach for probing relaxation processes and suppressing information associated with electrode polarization effects in dielectric spectra. The real part (M') quantifies the material's elastic response to an applied alternating electric field. Unlike the dielectric constant, which emphasizes capacitiveness (energy storage), the modulus provides sensitivity to conductivity relaxation and can reveal subtle features associated with charge carrier dynamics. An increase in modulus corresponds to decreases in permittivity and highlights the blocking of charge carrier motion. At low frequency, all samples show relatively low values of M'. Therefore, the electric field stimulates long-range ionic motion and polarization, which is reflected in the high permittivity and low modulus. At high frequency, the modulus (M') rises sharply, charge carriers cannot keep pace with rapid field oscillations, and relaxation manifests as reduced energy storage and increased elastic response. The curves approach their asymptotic values, indicating the complete suppression of electrode effects and maxed-out dielectric relaxation for each sample.

The pure blend shows the largest modulus at high frequency, signifying the strongest blocking effect and lowest permittivity (most rapid relaxation). In the absence of inorganic fillers, the system's flexibility and segmental motion enable charges to respond over broad frequency ranges. The modulus (M') increases at high-frequency points to a characteristic relaxation time, beyond which carriers become immobilized. The addition of MgO results in subdued M' growth and a lower plateau, demonstrating that the composite retains higher permittivity and less pronounced blocking over broad frequencies, where MgO acts as a nano-filler, which introduces interfacial regions that facilitate charge carrier movement and reduce relaxation propensity. The lesser rise in modulus suggests easier ionic transport and diminished blocking compared to the pure polymer. After adding Bi_2O_3, the curves for 10, 20, and 30 min were obtained by laser ablation; the modulus curves lie between those of the pure blend and the MgO-only composite. As ablation duration increases, plateau modulus values decrease slightly, indicating more effective charge relaxation or enhanced conductivity.

Fig. 11 illustrates the dependence of the imaginary component of the dielectric modulus (M'') on the logarithm of frequency ($\log f$) for the various polymer nanocomposite samples under investigation. The imaginary modulus (M'') represents a parameter for elucidating the dielectric relaxation phenomena in polymer blends and nanocomposites. As the out-of-phase response of the complex dielectric function, M'' enables the assessment of charge carrier dynamics, their relaxation times, and the influence of interfacial or surface effects in nanostructured systems. Plotting M'' *versus* $\log f$ permits a detailed analysis of both conduction mechanisms and the dielectric relaxation behavior intrinsic to each composite formulation.

Differences in dielectric response are observed among the tested materials. The pristine PVA/PEO blend exhibits a pronounced M'' peak at low frequencies (around $\log = 1$), which is succeeded by a gradual decline and the emergence of a broad plateau at higher frequencies ($\log f > 3$). This behavior typifies robust relaxation processes, potentially arising from polymer chain segmental dynamics and ionic motion within the blend matrix. The substantial height of the peak implicates

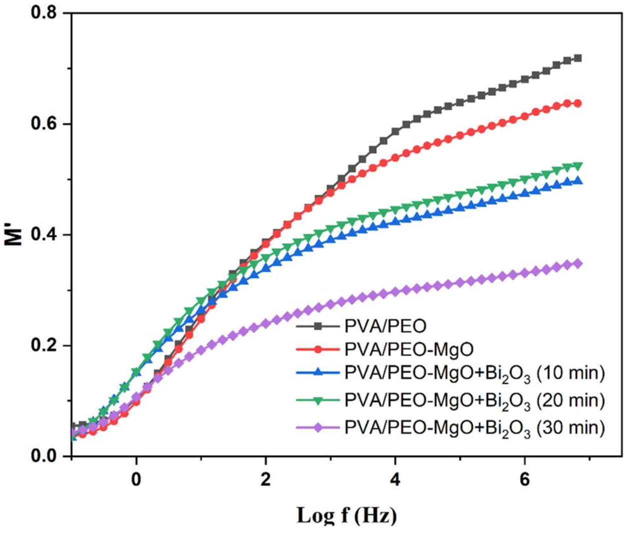

Fig. 10 Frequency dependence of the dielectric modulus (M') for PVA/PEO, PVA/PEO–MgO, and PVA/PEO–MgO–Bi_2O_3 nanocomposites.

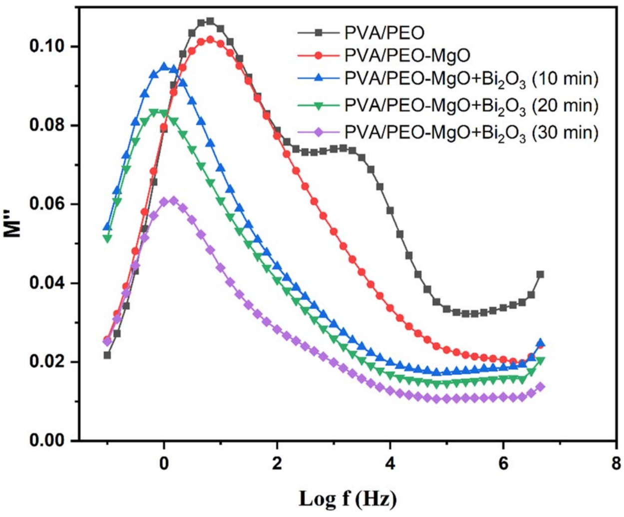

Fig. 11 Dependence of the dielectric modulus (M'') on the frequency ($\log f$) for PVA/PEO, PVA/PEO–MgO, and PVA/PEO–MgO–Bi_2O_3 nanocomposites.

high polarizability and slower relaxation dynamics in the absence of nanofiller additives.

After the introduction of MgO nanoparticles, a reduction in the amplitude of the M'' peak is evident alongside a shift toward lower frequencies. These findings indicate modified relaxation dynamics, where MgO may serve either as a charge trapping center or as a factor altering the nanostructure, thereby constraining charge carrier mobility and expediting the relaxation rate. The altered width and position of the relaxation peak demonstrate an evolution in the distribution of relaxation times, and the dielectric properties are enhanced relative to the unmodified blend.

The modification by Bi_2O_3 incorporation *via* laser ablation is reflected in progressive changes to the dielectric spectrum. As the duration of laser ablation increases from 10 to 30 minutes, a systematic decrease in the peak value of M'' is observed, and the peak position shifts to higher frequencies. At 10 minutes, the observed peak is similar in value to the MgO-only system yet remains below that of the original polymer blend. For the sample ablated for 20 minutes, the peak becomes broader and diminishes in magnitude. This broadening is characteristic of increased relaxation heterogeneity and reduced charge mobility. After 30 minutes, the peak is lowest, suggesting the greatest restriction of relaxation, enhanced polarization phenomena, or potentially the saturation of charge trapping within the system.

Bi_2O_3 nanoparticles significantly contributed to the polarization and conductivity of the prepared samples through several interrelated mechanisms. These nanoparticles facilitate charge transfer by enabling electron exchange between Bi 6s and O 2p orbitals and conduction band states, acting as localized charge-holding sites that can either enhance or restrict charge hopping depending on their size and dispersion within the polymer matrix. At shorter removal times, such as 10 minutes, the nanoparticles are less integrated and larger, allowing for relatively freer charge transfer, similar to MgO-only systems. As the removal time increases, improved dispersion and smaller nanoparticle size enhance interface coupling, increasing charge retention and reducing mobility, which results in lower dielectric loss peaks. The incorporation of Bi_2O_3 increases interface heterogeneity between the polymer chains and nanoparticles, with interface polarization resulting from charge accumulation at boundaries with different conductivity and permeability. With prolonged ablation, the increased homogeneity of the nanoparticles promotes multi-stage relaxation, wider relaxation peaks, and stronger local polarization effects. Charges are more effectively trapped due to the increased interfacial surface area and nanoparticle interactions with the polymer, restricting dipole relaxation and enhancing polarization saturation. Furthermore, the smaller, well-dispersed Bi_2O_3 nanoparticles formed after longer ablation periods enhance Maxwell–Wagner–Sillars polarization by increasing the interfacial surface area. This typically reduces long-range charge carrier mobility but increases local polarization. The reduced nanoparticle size also induces quantum size effects, altering the optical and electrical band gaps and modifying charge carrier density and mobility, which directly impact dielectric loss and conductivity. This interaction between charge transfer, interfacial polarization, and nanoparticle size and dispersion controls the insulating properties of the PVA/PEO–MgO–Bi_2O_3 composite, which evolves with excision time, effectively balancing conductivity and polarization.

The modifications in M'' spectra can be attributed to the combined effects of nanofiller presence and the degree of laser-induced cracking. MgO nanoparticles influence the local polymer matrix by creating additional charge trapping sites, which restrict carrier movement and amplify polarization effects, consistent with the Maxwell–Wagner–Sillars interfacial polarization mechanism. The addition of Bi_2O_3, a high-permittivity oxide, *via* laser ablation supports finer dispersion and stronger interaction with the polymer chains, leading to enhanced polarization and further suppression of the relaxation peak. Extended ablation times contribute to changes in particle size and surface area, promoting greater restriction of dielectric response and expedited relaxation phenomena.

All samples in the series display distinctive relaxation peaks at specific frequency intervals, indicating the frequency at which polarization mechanisms transition from synchronizing with the applied field to lagging behind it. At lower frequencies, sufficient time is available for atomic and molecular rearrangements, resulting in higher values of M''. As frequency increases, the lag between dipole reorientation and the applied field becomes more pronounced, causing a decrease in M'' and signifying faster dielectric relaxation and reduced energy dissipation. These results demonstrate how the sequential addition of MgO and Bi_2O_3 nanofillers, coupled with variable laser ablation durations, can systematically tailor the dielectric relaxation characteristics of PVA/PEO-based polymer nanocomposites, with clear implications for optimizing their performance in applications requiring a controlled dielectric response and low energy loss.

The Cole–Cole diagram (the relation between the real (M') and imaginary (M'') parts) for various PVA/PEO–MgO + Bi_2O_3 nanocomposite samples is shown in Fig. 12. A Cole–Cole plot (M' *vs.* M'') is used to analyze dielectric relaxation and distinguish between different polarization mechanisms.[31] A clear trend shows that the semi-arc peaks become lower and shift towards lower M' values as both additional fillers (Bi_2O_3) and prolonged processing times are incorporated. The pristine binary blend shows the largest arc, while the sample processed with MgO and Bi_2O_3 for 30 minutes displays the smallest arc. Each sample exhibits a semicircular arc, which is characteristic of Debye-type dielectric relaxation. The height and position of the arc provide insight into the relaxation strength and relaxation time distribution in the system. The PVA/PEO sample displays the largest semicircular arc. Its arc also extends furthest along the M' axis, indicating a relatively high relaxation modulus and substantial energy dissipation. This suggests that the binary blend has moderate chain mobility and polarization possibly due to the segmental dynamics of PVA and PEO chains and their interactive effects. Introducing MgO nanoparticles reduces both the maximum peak and the width along the M' axis. The reduction can be attributed to the restricted molecular mobility imposed by the filler, which introduces additional

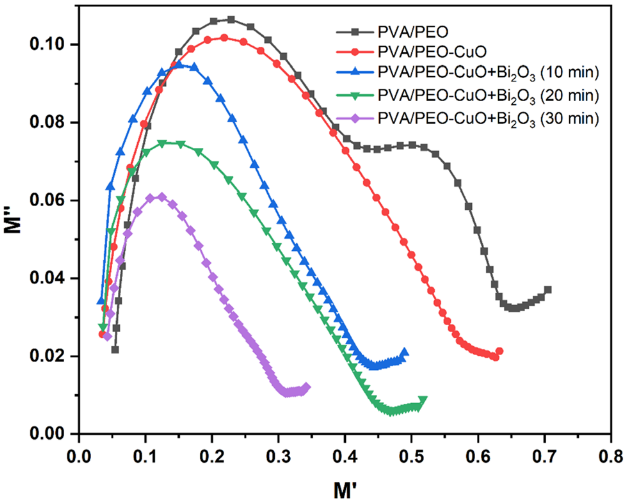

Fig. 12 Cole–Cole diagram (the relation between the real (M') and imaginary (M'')) for PVA/PEO, PVA/PEO–MgO, and PVA/PEO–MgO–Bi$_2$O$_3$ nanocomposites.

interfaces and micro-capacitances that hinder long-range segmental motion. The addition of Bi$_2$O$_3$ further decreases the peak height of the arc and shifts the arc to even lower M' values. The blue curve, representing the 10 minute processed sample, implies a further restriction in chain mobility or an enhancement in interfacial polarization, leading to a shorter relaxation time and less energy storage/dissipation at higher M' values.

Fig. 13 displays the variation in AC conductivity log(σ_{ac}) against frequency (log f) for pure PVA/PEO blend, PVA/PEO doped with MgO, and PVA/PEO–MgO and Bi$_2$O$_3$ (where Bi$_2$O$_3$ is doped by the duration of laser ablation processing (10, 20, and 30 minutes)). AC conductivity is measured across a range of frequencies and generally exhibits a frequency-dependent behavior well described by Jonscher's universal power law:[32,33]

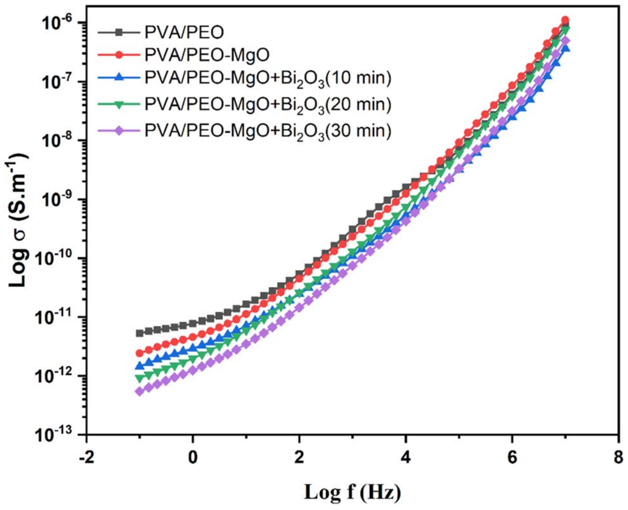

Fig. 13 Variation of AC conductivity log(σ_{ac}) against frequency (log f) for PVA/PEO, PVA/PEO–MgO, and PVA/PEO–MgO–Bi$_2$O$_3$ nanocomposites.

$$\sigma_{tot} = \sigma_{ac} + \sigma_{dc}, \tag{10}$$

where σ_{dc} is the DC conductivity. From the figure, all curves depict increasing AC conductivity with increasing log frequency. At low frequencies, conductivity is limited due to polarization processes, charge carrier trapping, and other relaxation mechanisms typical of polymers. As the frequency rises, these limitations are overcome; the oscillating field energizes more carriers to participate in conduction, resulting in a sharp increase in conductivity.

The PVA/PEO polymer matrix displays relatively high conductivity values at all frequencies. Its relatively high conductivity primarily arises from good segmental mobility within the highly amorphous polymer domains, which permit swift ionic movement. Conductivity in such blends is usually governed by the availability of free ions and the flexibility of polymer chains. Doping with MgO to the PVA/PEO blend, MgO acts in two major ways: (1) it enhances polymer amorphousness, breaking up ordered crystallite regions and freeing more chains for ion conduction. (2) It may introduce additional conduction pathways due to interfacial effects, creating localized regions where ions can hop more readily. The increased conductivity demonstrates the effectiveness of nano-filler additions in plasticized polymer. For the PVA/PEO–MgO + Bi$_2$O$_3$ samples, as laser ablation time increases, they show systematic decreases in conductivity, emphasizing the role of both filler type and laser processing time. For the short laser ablation (10 min) sample, the sample retains higher conductivity than those treated for longer times, suggesting minimal disruption to conduction pathways and possible enhancement from optimal filler dispersion. The lowest overall conductivity is observed after adding Bi$_2$O$_3$ at 10 min and 30 min of laser ablation. Extended ablation may severely alter the composite structure, increasing defects, creating dead ends for conductivity, or generating excessive interfaces that trap or immobilize charge carriers.

This conductivity suppression reflects a key principle: although inorganic fillers and laser processing can enhance material performance, their benefits are subject to intricate trade-offs. Excessive filler loading, poor dispersion, or over-processing can prevent charge carriers from moving freely, counteracting the intended advantages.

4. Conclusion

This study successfully developed PVA/PEO-based polymer nanocomposites reinforced with MgO and Bi$_2$O$_3$ nanoparticles, fabricated by pulsed laser ablation, demonstrating a clear correlation between ablation time and overall material performance. Structural characterization using X-ray diffraction (XRD) confirmed improved crystallinity and successful incorporation of both oxides into the polymer matrix. The FTIR results indicated strong interfacial bonding between the nanoparticle surfaces and the polymer functional groups. The ultraviolet-diffuse reflectance spectroscopy (UV-DRS) revealed tunable optical behavior, with increased absorbance and red-shifted absorption edges at longer ablation times, indicating improved nanoparticle dispersion and crystallinity. TGA revealed a significant enhancement in thermal stability. The PVA/PEO–MgO–Bi_2O_3 composite, excised for 30 min, exhibited the highest decomposition temperature and the largest amount of char residue, confirming the synergistic barrier and cross-linking effects of the dual fillers. Dielectric conductivity and AC measurements showed frequency-dependent polarization, which is consistent with the Maxwell–Wagner–Sillars mechanism, with prolonged excimer time, resulting in a decrease in the dielectric constant and electrical conductivity due to optimized particle dispersion and charge carrier confinement. The gradual increase in nanoparticle homogeneity with excimer time effectively improved the interface polarization, relaxation dynamics, and energy dissipation properties. The incorporation of MgO and Bi_2O_3 nanoparticles *via* laser excimer provides a versatile route for tuning the structural, optical, and electrical properties of biodegradable polymer composites. The results demonstrate that controlled removal time is a key factor influencing nanoparticle morphology, interface bonding, and functional response, enabling precise tuning of thermal stability and dielectric behavior. These findings position PVA/PEO–MgO–Bi_2O_3 nanocomposites as promising materials for multifunctional applications.

Author contributions

I. S. Elashmawi: formal analysis, investigation, and writing – original draft. A. A. Menazea: methodology, formal analysis, investigation, writing – original draft, and writing – review & editing.

Conflicts of interest

The authors declared that they have no conflict of interest.

Data availability

Data will be available from the corresponding author upon reasonable request.

References

1 Z. W. Abdullah, Y. Dong, I. J. Davies and S. Barbhuiya, *Polym.-Plast. Technol. Eng.*, 2017, **56**(12), 1307–1344.
2 B. Eslami, I. Ghasemi and M. Esfandeh, *Polymers*, 2023, **15**(14), 3063.
3 A. L. Waly, A. M. Abdelghany and A. E. Tarabiah, *J. Mater. Res. Technol.*, 2021, **14**, 2962–2969.
4 R. Agarwal, M. S. Alam and B. Gupta, *J. Appl. Polym. Sci.*, 2013, **129**(6), 3728–3736.
5 B. Gupta, R. Agarwal and M. S. Alam, *J. Appl. Polym. Sci.*, 2013, **127**(2), 1301–1308.
6 J. Wang, J. Liang, L. Sun and S. Gao, *Chemosphere*, 2019, **219**, 130–139.
7 T. S. Soliman, M. F. Zaki, M. M. Hessien and S. I. Elkalashy, *Opt. Mater.*, 2021, **111**, 110648.
8 J. Y. Shin, D. Y. Lee, J. I. Yoon and Y. S. Song, *Macromol. Res.*, 2020, **28**(9), 813–819.
9 P. Basu, A. Repanas, A. Chatterjee, B. Glasmacher, U. NarendraKumar and I. Manjubala, *Mater. Lett.*, 2017, **195**, 10–13.
10 C. Wang, Z. Wen, W. Chen, J. Cao, X. Wang, F. Zhou, B. Li, K. Wu and Q. Liu, *ChemSusChem*, 2025, **18**(17), e202500445.
11 H. Wang, C. Lin, X. Yan, A. Wu, S. Shen, G. Wei and J. Zhang, *J. Electroanal. Chem.*, 2020, **869**, 114156.
12 H. M. Ragab, *J. Mater. Sci.: Mater. Electron.*, 2022, **33**(25), 19793–19804.
13 A. M. Abdelghany, I. S. Elashmawi, A. A. Al-Shamari and H. Alnattar, *J. Mater. Sci.: Mater. Electron.*, 2023, **34**(5), 388.
14 Y. Eom, B. Choi and S. I. Park, *J. Polym. Environ.*, 2019, **27**(2), 256–262.
15 S. Kwon, Y. Kim, H. Jang, S. J. Kim and S. I. Park, *J. Appl. Polym. Sci.*, 2023, **140**(2), e53299.
16 R. Strapasson, S. C. Amico, M. F. R. Pereira and T. H. D. Sydenstricker, *Polym. Test.*, 2005, **24**(4), 468–473.
17 P. H. C. Camargo, K. G. Satyanarayana and F. Wypych, *Mater. Res.*, 2009, **12**, 1–39.
18 C. I. Idumah, A. Hassan and D. E. Ihuoma, *Polym.-Plast. Technol. Mater.*, 2019, **58**(10), 1054–1109.
19 A. H. Alshammari, *Polymers*, 2024, **16**(10), 1392.
20 W. Jiang, S. Xu, C. Lv, D. Lan, S. Zhang, Z. Gao, Z. Jia and G. Wu, *Carbon*, 2025, 120784.
21 C. Jia, F. Zhang, Z. Wang, C. Lv, D. Lan, S. Zhang, Z. Jia, Z. Gao and G. Wu, *Compos. Commun.*, 2025, 102569.
22 W. Zhao, Z. Guo, D. Lan, Z. Jia, S. Zhang and G. Wu, *Small*, 2025, **21**(45), e09339.
23 S. El-Gamal and A. M. El Sayed, *J. Compos. Mater.*, 2019, **53**(20), 2831–2847.
24 A. M. Alshehri, A. Almalki, A. A. Menazea and M. A. El-Morsy, *Mater. Chem. Phys.*, 2025, **340**, 130657.
25 M. El-Sharnouby, A. E. Askary, N. S. Awwad, H. A. Ibrahium, M. E. Moustapha, M. O. Farea and A. M. Abdelghany, *J. Inorg. Organomet. Polym. Mater.*, 2022, **32**(6), 2269–2278.
26 N. M. Basfer, *J. Non-Cryst. Solids*, 2023, **621**, 122619.
27 A. M. El-Naggar, Z. K. Heiba, A. M. Kamal and M. B. Mohamed, *Opt. Quant. Electron.*, 2023, **55**(7), 609.
28 I. S. Elashmawi, N. S. Alatawi and N. H. Elsayed, *Results Phys.*, 2017, **7**, 636–640.
29 N. S. Alghunaim, *Results Phys.*, 2015, **5**, 331–336.
30 I. S. Elashmawi, E. M. Abdelrazek, A. M. Hezma and A. Rajeh, *Phys. B*, 2014, **434**, 57–63.
31 M. A. Morsi, E. M. Abdelrazek, R. M. Ramadan, I. S. Elashmawi and A. Rajeh, *Polym. Test.*, 2022, **114**, 107705.
32 S. F. Chérif, A. Chérif, W. Dridi and M. F. Zid, *Arab. J. Chem.*, 2020, **13**(6), 5627–5638.
33 H. A. Alsalmah, A. Rajeh and O. Nur, *Ceram. Int.*, 2024, **50**(7), 12167–12174.